Draft version November 4, 2025
Typeset using LaTeX twocolumn style in AASTeX7.0.1

Bridging Theory and Observation: Synthetic FIR Insights into Star Formation Efficiency

Alexander Escamilla,[1] Michael Y. Grudić,[2] and Anna L. Rosen[1,3]

[1] Department of Astronomy, San Diego State University, San Diego, CA 92182, USA
[2] Center for Computational Astrophysics, Flatiron Institute, New York, NY 10010, USA
[3] Computational Science Research Center, San Diego State University, San Diego, CA 92182, USA

(Received September 20, 2025; Revised; Accepted)

Submitted to ApJ

ABSTRACT

The star formation efficiency per free-fall time ($\epsilon_{\rm ff}$) quantifies how efficiently giant molecular clouds (GMCs) convert gas into stars, and is often observed to be orders of magnitude lower than expected for free-fall collapse. Observers typically estimate $\epsilon_{\rm ff}$ by mapping FIR dust emission to infer gas surface densities ($\Sigma_{\rm gas}$) and counting embedded protostars, assuming simplified lifetimes and masses. Using the fiducial STARFORGE radiation–magnetohydrodynamics simulation of a $M_{\rm cl} = 2 \times 10^4 \, M_\odot$ GMC that self-consistently models star cluster formation and stellar feedback, we generate synthetic far-infrared (FIR) observations and apply the same methodologies used in GMC surveys to investigate this discrepancy. We present the first $\epsilon_{\rm ff}$–$\Sigma_{\rm gas}$ analysis in a fully feedback-regulated GMC simulation that resolves the formation of individual stars. Our synthetic measurements reproduce the low observationally inferred efficiencies, showing that feedback-regulated star formation naturally produces $\epsilon_{\rm ff} \sim$ 1–3% without requiring extreme initial conditions. We also find that $\epsilon_{\rm ff}$ varies strongly over a GMC's lifetime, suggesting that much of the observed scatter reflects evolutionary sampling rather than intrinsic cloud-to-cloud differences. Finally, by comparing observational and theoretical definitions, we show that methodological assumptions introduce systematic biases. A transition near $\log \Sigma_{\rm gas} \approx 2.6, {\rm M}_\odot, {\rm pc}^{-2}$ marks where observers overestimate free-fall times at low densities and underestimate star formation rates at high densities.

Keywords: Star formation (1569); Star forming regions (1565);Giant molecular clouds (653); Protostars (1302); Young stellar objects (1834); Early stellar evolution (434); Far infrared astronomy (529); Infrared astronomy (786); Dust continuum emission (412); Magnetohydrodynamical simulations (1966)

1. INTRODUCTION

Star formation is a fundamental process that shapes the structure and evolution of galaxies, sets the properties of star clusters, and the initial conditions for planet formation (C. F. McKee & E. C. Ostriker 2007). Despite its importance, the physical mechanisms regulating the conversion of cold, dense interstellar gas into stars remain elusive due to the complex interplay of multiple physical processes, including magnetic fields, turbulence, and stellar feedback that act within giant molecular clouds (GMCs) before they ultimately collapse into protostars (E. A. Bergin & M. Tafalla 2007; P. Padoan et al. 2014). These mechanisms operate across many scales, making star formation a complex, nonlinear physical process.

One of the most challenging aspects of studying star formation is the extended lifetimes of GMCs ($\geq 10\,$Myr), which makes it difficult to obtain a complete picture of star formation from observations alone. Thus, a convenient way to quantify cloud-scale star formation is through the star formation efficiency per free-fall time, $\epsilon_{\rm ff}$, a dimensionless measurement that indicates the fraction of a cloud's mass that is converted to stars during one gravitational free-fall time:

$$\epsilon_{\rm ff} = \frac{\dot{M}_\star}{M_{\rm gas}/t_{\rm ff}}, \tag{1}$$

Corresponding author: Alexander Escamilla
alex.escamilla2244@gmail.com

where $\dot{M}_\star$ is the star formation rate (SFR), $M_{\rm gas}$ is the GMC mass, and $t_{\rm ff}$ is the cloud gravitational free-fall time.

$\epsilon_{\rm ff}$ has historically exhibited a persistent mismatch between theoretical predictions and observational measurements (M. R. Krumholz 2014). B. Zuckerman & I. Evans (1974) first identified this discrepancy, measuring values of $\epsilon_{\rm ff} \leq 1\%$. In comparison, idealized theoretical models that only accounted for gravity predicted efficiencies of order 100% from clouds (P. Goldreich & J. Kwan 1974). These results suggested either observational biases or missing physical mechanisms, such as turbulence (M.-M. Mac Low & R. S. Klessen 2004), magnetic fields (C. Federrath & R. S. Klessen 2013), and stellar feedback – the injection of energy and momentum into the ISM by young stars (J. E. Dale 2015; M. Y. Grudić et al. 2019). Since then, several studies have demonstrated how these mechanisms suppress gravitational collapse and regulate the conversion of interstellar gas into stars (M. Y. Grudić et al. 2022; A. L. Rosen & M. R. Krumholz 2020; S. M. Appel et al. 2023). However, these models must be compared with observations directly to determine which of these physical mechanisms is primarily responsible for inefficient star formation in star-forming clouds.

None of the quantities in Eq. (1) — the stellar accretion rate, total gas mass, free-fall time, and the gas density — are directly measurable, or even well-defined in realistic systems with substructure and line-of-sight blending. Consequently, observers must infer $\epsilon_{\rm ff}$ through indirect methods, which primarily include: counting young stellar objects (YSOs), assuming average YSO lifetimes and masses, and adopting geometric assumptions about cloud structure to estimate $t_{\rm ff}$ (I. Evans et al. 2009; M. M. Dunham et al. 2014; R. Pokhrel et al. 2021; Z. Hu et al. 2022). Observational studies of star formation depend on far-infrared (FIR) surveys to identify embedded protostars by tracking FIR emission from dust heated by young stars. This approach yields maps of star-forming regions and estimates of gas surface densities. Molecular gas mass is inferred from FIR dust emission by converting the inferred dust column densities and adopting a dust-to-gas ratio (I. Evans et al. 2009; S. I. Sadavoy et al. 2013; R. A. Gutermuth et al. 2009). Each step introduces uncertainties affecting the molecular gas estimates used to calculate GMC masses and free-fall timescales. Additionally, background active galactic nuclei (AGN) contamination can skew YSO counts, leading to inflated SFRs. This complicates the interpretation of whether observed variations in $\epsilon_{\rm ff}$ stem from intrinsic physical differences or result from observational biases and simplified assumptions.

In contrast, high-fidelity numerical simulations provide the "ground truth" by capturing the evolution of gas and stars in a GMC, thereby enabling a more comprehensive analysis of $\epsilon_{\rm ff}$ (T. J. Haworth et al. 2018). Previous simulation studies have addressed this challenge by recovering $\epsilon_{\rm ff}$ from synthetic observables. Early work by S. S. R. Offner et al. (2009) demonstrated that radiative feedback from protostars heats the surrounding gas in star-forming regions and reduces unrealistically high $\epsilon_{\rm ff}$ toward more observationally consistent values, establishing stellar feedback as a regulatory mechanism; however, that study only included radiative feedback, neglected other forms of stellar feedback (e.g., protostellar outflows), and did not capture the formation of high-mass stars. Most recently, P. Suin et al. (2024) examined individual feedback mechanisms in separate simulations, finding that different feedback mechanisms ultimately reduced theory–observation discrepancies in $\epsilon_{\rm ff}$, but did not self-consistently capture individual star formation due to resolution constraints. These limitations highlight the need for a high-resolution simulation suite capable of capturing individual star formation on cloud scales and that includes all major feedback processes inherent to star formation.

Quantifying the degree to which observational biases versus intrinsic physical processes drive the observed discrepancies remains an open question. Thus, a direct comparison between observational and theoretical approaches is needed to untangle the source of this discrepancy. In this study, we generate synthetic FIR observations from a radiation-magnetohydrodynamics (RMHD) star formation simulation suite, thereby enabling a controlled test to determine how systematic observational biases affect the inferred values of $\epsilon_{\rm ff}$. We use STARFORGE, a simulation framework implemented in GIZMO (P. F. Hopkins 2017). STARFORGE self-consistently incorporates all major stellar feedback processes while resolving the initial mass function (IMF) down to $0.1\,{\rm M}_\odot$ on GMC scales (M. Y. Grudić et al. 2022).

While M. Y. Grudić et al. (2022) measured the global $\epsilon_{\rm ff}$, a detailed analysis of the $\epsilon_{\rm ff} - \Sigma_{\rm gas}$ relationship has not yet been performed. We address this gap by producing synthetic FIR observations of the STARFORGE simulation suite and present the first $\epsilon_{\rm ff} - \Sigma_{\rm gas}$ test in a full-feedback GMC by directly comparing our observationally resolved estimates of $\epsilon_{\rm ff}$ against the simulations' intrinsic values throughout its evolution. We follow the observational methodology introduced by R. Pokhrel et al. (2021), which found that different surface density thresholds lead to variations in $\epsilon_{\rm ff}$ across star-forming GMCs. Any discrepancies that persist af-

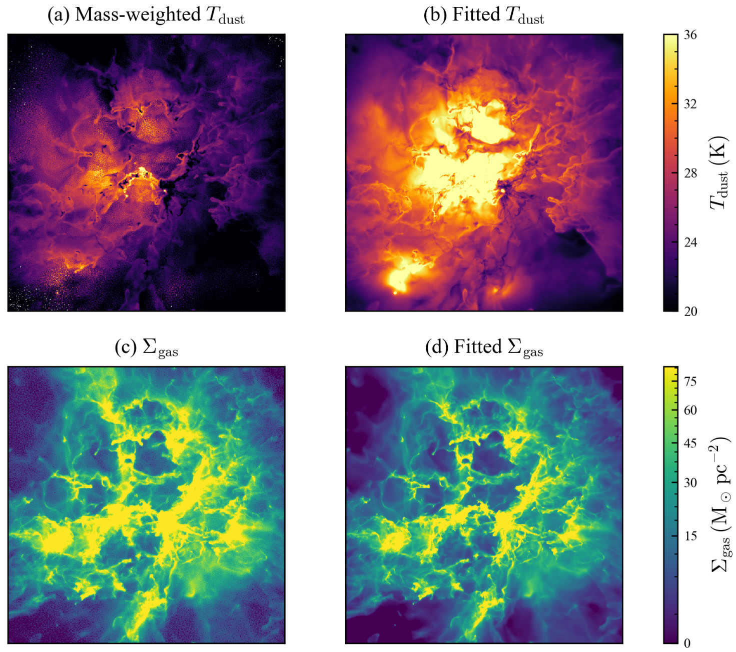

Figure 1. Comparison of intrinsic STARFORGE dust properties with fitted values from our synthetic observations. (a) Mass-weighted dust temperature $T_{\rm dust}$ from the simulation. (b) Fitted $T_{\rm dust}$ recovered from SED modeling. (c) Intrinsic gas surface density $\Sigma_{\rm gas}$. (d) Fitted $\Sigma_{\rm gas}$ derived from $500\,\mu$m optical depth assuming a 1% dust-to-gas ratio. While SED fitting slightly overestimates dust temperatures, it reproduces the cloud morphology and yields reasonable surface density estimates, demonstrating the reliability of our synthetic observation pipeline.

ter applying these methods may indicate missing physical processes in the STARFORGE simulations. This approach also aids in determining how factors like spatial resolution and AGN contamination influence measurements of $\epsilon_{\rm ff}$. We then examine variables such as cloud evolutionary stage, line-of-sight resolution, choice of methodology, and projected contamination may affect trends in the observationally-inferred values of $\epsilon_{\rm ff}$, and investigate whether such variations arise from the underlying physics and evolution, or are primarily due to observational limitations.

The structure of this paper is as follows: Section 2 describes the numerics and synthetic observation pipeline employed on the simulated snapshots. Section 3 presents our main findings, Section 4 discusses their implications for interpreting observed star formation efficiencies, and lastly Section 5 presents our conclusions.

2. METHODS

2.1. *Simulations*

We conduct our analysis using STARFORGE, a star formation simulation framework built on GIZMO, a magnetohydrodynamics (MHD) code that employs a mesh-free, Lagrangian finite mass method to solve the equations of ideal MHD (P. F. Hopkins & M. J. Raives 2016; P. F. Hopkins 2017) coupled with self-gravity, stellar dynamics, and multi-band radiative transfer. STARFORGE incorporates key stellar feedback processes that includes: stellar irradiation, thermal re-emission by interstellar dust, protostellar outflows, stellar winds, and supernovae (M. Y. Grudić et al. 2022). Protostars are modeled as accreting sink particles tied to a sub-grid protostellar evolution model following the methods described in S. S. R. Offner et al. (2009). This setup allows a multi-physics approach that captures self-consistent star formation, stellar feedback, and global GMC dynamics.

We used the fiducial run from the STARFORGE suite designed to model typical Milky Way GMCs. The initial conditions include a turbulent cloud with a mass of $2 \times 10^4\,\mathrm{M_\odot}$ and a radius of $\approx 10\,$pc, giving a mean surface density of $\Sigma_{\rm gas} = M/\pi R^2 = 64\,\mathrm{M_\odot pc^{-2}}$ consistent with measurements from nearby GMCs (M. Heyer et al. 2009; C. J. Lada et al. 2010). This simulation reproduces key observational benchmarks, including the stellar initial mass function (IMF; N. Bastian et al. 2010) and the observed star formation efficiency per free-fall time, $\epsilon_{\rm ff}$. Here we summarize the initial conditions; for a full description, see M. Y. Grudić et al. (2022). The GMC is embedded in a low-density ambient medium within a 100 pc simulation box to minimize boundary effects.

An initial random supersonic turbulent velocity field with a power-law spectrum, $P(k) \propto k^{-2}$, is imposed on the cloud and scaled to yield a virial parameter

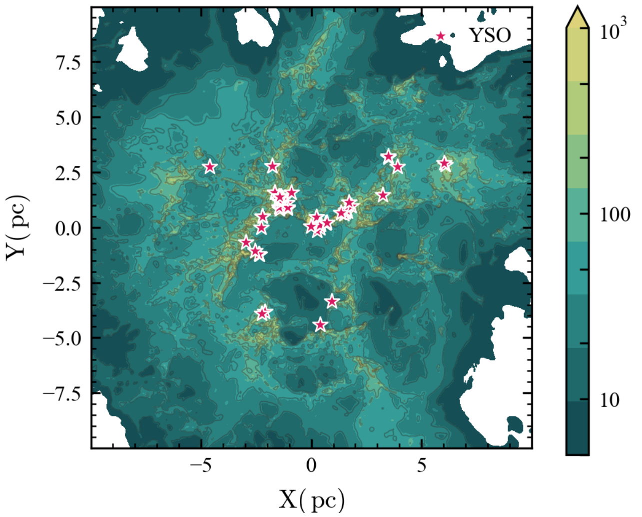

Figure 2. Sample synthetic observation of a snapshot of our fiducial simulation. The color scale represents gas surface density in units of $\mathrm{M_\odot\,pc^{-2}}$. Overlaid contours trace the density structures and show the apertures used to compute $\epsilon_{\rm ff}$. Magenta stars denote young stellar objects (YSOs), which predominantly form within the densest regions of the cloud.

$\alpha_{\rm turb} \approx 2$ at initialization, where $\alpha_{\rm turb} = \frac{5R\sigma^2}{3GM}$. A uniform magnetic field is imposed to produce an initial mass-to-flux ratio of $\mu \approx 1.3$ (T. C. Mouschovias & L. Spitzer 1976), so the cloud is magnetically supercritical, consistent with observational constraints (R. M. Crutcher 2012). The simulation has a mass resolution of 10^{-3} $\mathrm{M_\odot}$ per gas element. Sink particles, representing individual protostars, are introduced once all sink formation criteria are satisfied, following M. Y. Grudić et al. (2021). Each sink particle evolves according to the subgrid protostellar model calibrated by S. S. R. Offner et al. (2009), which updates the protostar's mass, radius, and luminosity based on its accretion history. These protostellar properties are inputs to the subgrid stellar feedback models that include radiative feedback, photoionization, bipolar outflows, and stellar winds. (M. Y. Grudić et al. 2021).

As the simulation evolves, the initial gravitational collapse of the GMC leads to the formation of dense cores that collapse to form protostars. These protostars inject momentum and energy into the interstellar medium (ISM) as they accrete mass, altering the cloud's structure, slowing collapse, and eventually dispersing the cloud (M. Y. Grudić et al. 2022). The simulation is evolved until it is disrupted by feedback, which occurs at $\approx 10\,$Myr (≈ 2.5 free-fall times).

2.2. *Synthetic Observations and Radiative Transfer*

We generate synthetic dust emission maps at FIR wavelengths of 150, 250, 350, and 500 μm to match observational surveys conducted with the SPIRE instrument of the Herschel Space Observatory (R. Pokhrel et al. 2016) by post-processing the 3D density and temperature distributions from the simulation, solving the time-independent radiative transfer equation given by:

$$\hat{\Omega} \cdot \nabla I_\nu(\mathbf{r}, \hat{\Omega}) = -\,\kappa_\nu(\mathbf{r})\,\rho(\mathbf{r})\,I_\nu(\mathbf{r}, \hat{\Omega}) + \kappa_\nu(\mathbf{r})\,\rho(\mathbf{r})\,B_\nu(T) \quad (2)$$

where I_ν is the specific intensity, κ_ν is the dust opacity, ρ is the gas density, and $B_\nu(T)$ is the Planck function (B. S. Hensley & B. T. Draine 2023).

Assuming optically-thin thermal emission from interstellar dust, we use a modified blackbody model to generate our gas surface-density maps per (R. Pokhrel et al. 2016):

$$I_\nu = \kappa_0 \left(\frac{\nu}{\nu_0}\right)^\beta B_\nu(T)\Sigma_{\rm gas} \quad (3)$$

where $\Sigma_{\rm gas}$ is the gas surface density, $\beta = 1.8$ is the fixed emissivity index, and κ_0 is the reference opacity from the Astrodust+PAH model (B. S. Hensley & B. T. Draine 2023). A dust-to-gas ratio of 1% is assumed throughout, consistent with observational SED fitting techniques applied to Herschel data (M. J. Griffin et al. 2010). Integrating Eq. (3) along each line of sight yields our synthetic maps. Our synthetic observations achieve a maximum spatial resolution of $0.01\,$pc $\approx 2000\,$AU. These maps reproduce the overall cloud morphology and yield reasonable gas surface densities when compared against the simulation's intrinsic values, validating our synthetic observation pipeline (Figure 1).

2.3. *Identification and Analysis of Young Stellar Objects*

Sink particles represent protostars in the simulation, and each particle is characterized by a unique spatial location, mass, and physical properties. To correlate SFRs directly with local gas densities similar to those employed by observational studies, we measure the observed gas surface density inferred by our mock observations at the nearest pixel to each Class 0 YSO, which we take to be protostars younger than 0.5 Myr. This classification aligns with observationally based protostellar definitions used in the YSO catalog derived from Spitzer observations by R. Pokhrel et al. (2021). Protostars younger than this threshold correspond to deeply embedded sources characterized by high envelope densities and substantial FIR emission due to their heavily dust-obscured environments. Class 0 represents the earliest

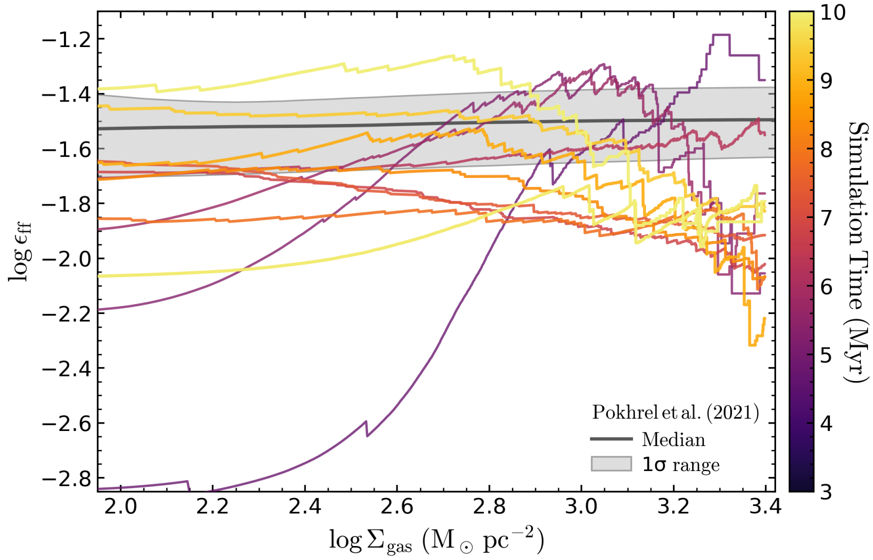

Figure 3. $\epsilon_{\rm ff}$ versus $\Sigma_{\rm gas}$ for the fiducial GMC over $\sim$10 Myr ($\approx 2.5\, t_{\rm ff}$). Colors show the evolutionary stage from early (purple) to late (yellow). Efficiencies start very low, rise sharply in the first 3–5 Myr, form a brief plateau near 5 Myr then decrease at higher $\Sigma_{\rm gas}$, flatten with mild declines at 6–7 Myr (orange/red), and show a stronger decrease at high densities by 8–10 Myr (yellow) as feedback disperses the cloud. The gray band indicates the 1σ scatter of Milky Way GMCs from R. Pokhrel et al. (2021), with a solid line of the median.

stage of protostellar evolution, typically ranging from approximately 0.1 to 0.5 Myr (M. M. Dunham et al. 2014). To address potential AGN contamination in FIR surveys, we inject synthetic AGN into our YSO catalog at a rate of $9\,\rm deg^{-2}$ (R. Pokhrel et al. 2020). We place the cloud at a distance of 0.6 kpc, the median of the cloud distances covered in the study by R. Pokhrel et al. (2021), which sets the angular size of the field on the sky, and draw the number of AGN from a Poisson distribution with $\lambda = A_{\rm field} \times 9\,\rm deg^{-2}$, where $A_{\rm field}$ is the projected sky area of the box from our simulation.

2.4. *Measuring Star Formation Efficiency*

We calculate $\epsilon_{\rm ff}$ from our synthetic dust emission maps and YSO catalogs, following the observational methods employed in R. Pokhrel et al. (2021). In this approach, the SFR is estimated as

$$\dot{M}_\star \; = \; \frac{N_{\rm YSOs}\langle M_{\rm YSO}\rangle}{\langle t_{\rm YSO}\rangle} \qquad (4)$$

where $N_{\rm YSOs}$ is the number of Class 0 YSOs within the defined contour, and $\langle M_{\rm YSO}\rangle = 0.5\,\rm M_\odot$, following previous observational estimates (M. M. Dunham et al. 2014; I. Evans et al. 2009) and consistent with the peak of the IMF (G. Chabrier 2005; P. Kroupa 2002). With both $\langle M_{\rm YSO}\rangle$ and $\langle t_{\rm YSO}\rangle$ treated as constants, with the SFR scaling directly with $N_{\rm YSOs}$.

The gravitational free-fall time within each contour is then

$$t_{\rm ff} = \sqrt{\frac{3\pi}{32 G\rho}} \qquad (5)$$

where we assume the gas enclosed by each surface density contour forms a sphere. Following M. R. Krumholz et al. (2012), the line-of-sight dimension is taken to be comparable to the projected size of the contour, giving

$$\rho = \frac{3\sqrt{\pi}\, M_{\rm gas}}{4\, A^{3/2}} \qquad (6)$$

where G is the gravitational constant, $M_{\rm gas}$ is the enclosed gas mass, ρ the mean density, and A the projected area of the contour. An example of the synthetic observation of our gas cloud is shown in Figure 2.

3. RESULTS

3.1. *Star Formation Efficiency vs. Gas Surface Density*

We present the main result of our work in Figure 3, where we replicate observational trends from R. Pokhrel et al. (2021). The gray shaded band shows the 1σ scatter of their GMC sample and a solid line of their median against our fiducial GMC values. We estimate Equation (1) using (4) and (5), turning it into an observational methodology at multiple surface density thresholds ($\Sigma_{\rm gas} \sim 100 - 1000\,\rm M_\odot\,pc^{-2}$) for several snapshots taken from the full simulation timeline ($\approx$ 10 Myr). From our synthetic observations, this figure demonstrates our inferred values of $\epsilon_{\rm ff}$. We find that $\epsilon_{\rm ff}$ varies both spatially and temporally with $\Sigma_{\rm gas}$ across the GMC with values ranging from 0.16% to 5.6%, with the majority of our estimates occurring between $1-3\%$

in agreement with the expected values inferred from observations

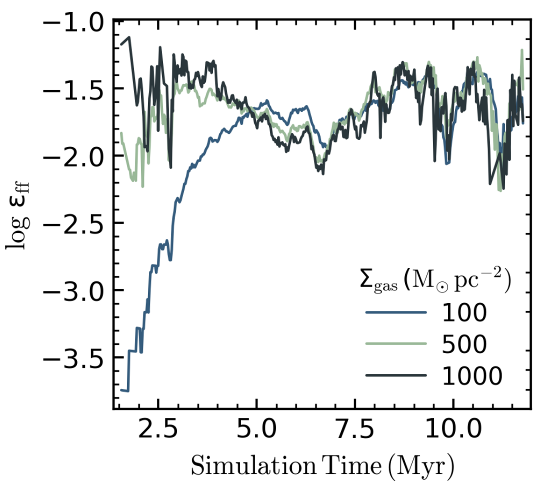

Figure 4. $\epsilon_{\rm ff}$ versus simulation time for a GMC at fixed surface density thresholds of $\Sigma_{\rm gas} = 100$ (blue), 500 (green), and $1000\,{\rm M_\odot\,pc^{-2}}$ (black). The low-density threshold shows a delayed rise in the first 2–3 Myr, while higher thresholds increase earlier. By ∼5 Myr, the curves become increasingly similar and evolve in parallel, then show episodic variability with comparable peaks, reaching efficiencies of ∼5%. This demonstrates that efficiency is set by the cloud's evolution rather than simply the amount of gas enclosed.

We find that the variation of $\epsilon_{\rm ff}$ across $\Sigma_{\rm gas}$ is most pronounced at early times. In the first 3–5 Myr (purple lines), $\epsilon_{\rm ff}$ is very low (≈ 0.3–0.5%) at low $\Sigma_{\rm gas}$ and rises steeply toward higher values, producing a brief plateau by ∼ 5 Myr before decreasing at the highest densities. Between 6–7 Myr (orange/red lines), the relation flattens across most $\Sigma_{\rm gas}$ and shows a mild downward trend in denser regions. By late times (8–10 Myr; yellow lines), $\epsilon_{\rm ff}$ remains steady across most $\Sigma_{\rm gas}$ but exhibits a more pronounced decline at the highest surface densities as feedback disperses the cloud.

3.2. *Time Dependence of Star Formation Efficiency*

Figure 4 shows the temporal evolution of $\epsilon_{\rm ff}$ at three fixed $\log \Sigma_{\rm gas}$ thresholds: 100, 500, and $1000\,{\rm M_\odot\,pc^{-2}}$. All three curves share a similar overall evolution. The low-density threshold ($\Sigma_{\rm gas} = 100\,{\rm M_\odot\,pc^{-2}}$; blue line) shows distinct behavior early on, with a delayed rise by nearly an order of magnitude over the first 2–3 Myr. In contrast, the higher thresholds ($\Sigma_{\rm gas} = 500$, $1000\,{\rm M_\odot\,pc^{-2}}$; green and black) follow consistent early-time trends with higher initial efficiencies. At intermediate times (t ∼ 3–7 Myr), $\epsilon_{\rm ff}$ stabilizes and the curves become increasingly similar, evolving in parallel, exhibiting episodic variability with comparable peaks and dips, reaching maximum efficiencies of about 5%.

3.3. *Effect of Resolution*

To determine how spatial resolution affects our $\epsilon_{\rm ff}$ measurements, we analyze our synthetic observations at three physical resolutions: 0.01 pc (STARFORGE default), 0.04 pc, and 0.08 pc, with the latter chosen to match the effective resolution of Herschel/SPIRE observations of nearby GMCs (M. J. Griffin et al. 2010; R. Pokhrel et al. 2020). Figure 5 shows $\log \epsilon_{\rm ff}$ versus $\log \Sigma_{\rm gas}$ for the three resolutions. We find that decreasing spatial resolution consistently reduces the inferred $\epsilon_{\rm ff}$. All three resolution values exhibit consistent trends at lower surface densities ($\log \Sigma_{\rm gas} < 2.8\,{\rm M_\odot\,pc^{-2}}$), with values centering around $\log \epsilon_{\rm ff} \sim -1.70$. However, the different resolutions diverge significantly at higher values of $\Sigma_{\rm gas}$.

3.4. *AGN Injection*

To explore how AGN contamination affects the inferred $\epsilon_{\rm ff}$, we inject synthetic AGN into our YSO catalogs using the method described in Section 2.2. This simulates the observational scenario where background AGN are misidentified as YSOs within a GMC. Figure 6 shows $\epsilon_{\rm ff}$ versus $\Sigma_{\rm gas}$ for different assumed cloud distances (0.1–1.6 kpc) from a sample simulation snapshot at t ≈ 6 Myr, along with a statistical 1σ spread computed over 24 randomized AGN-injection realizations per distance.

The largest spread is seen at 0.1–0.4 kpc, with $\epsilon_{\rm ff}$ offset by up to ∼ 0.1 dex at low surface densities ($\log \Sigma_{\rm gas} \lesssim 2.5\,{\rm M_\odot\,pc^{-2}}$). At larger distances the spread decreases, and by 1 kpc the curves show only minor differences, with values remaining similar across the surface density range.

4. DISCUSSION

In this work, we generated and analyzed mock FIR observations of STARFORGE's fiducial star cluster formation simulation suite to reproduce the observationally-inferred values of the star formation efficiencies ($\epsilon_{\rm ff}$) of star-forming environments following the methods of R. Pokhrel et al. (2021). This approach allowed us to the bridge the gap between theoretical predictions taken directly from our simulated outputs and those inferred via protostellar counts and mass estimates via FIR observations. Our results demonstrate that $\epsilon_{\rm ff}$ varies across a cloud's lifetime and that stellar feedback is an important mechanism to regulate star formation in dense gas at late stages of the star formation process.

Numerous simulations have demonstrated that stellar feedback is a key mechanism in regulating star formation

Table 1. Alternate representations of $\epsilon_{\rm ff} = {\rm SFR}/{\rm GDR}$. We list each variant's definition of star formation rate (SFR) and gas depletion rate (GDR).

Variant	Star Formation Rate (SFR)	Gas Depletion Rate (GDR)
Observational	$\mathrm{SFR_{Obs}} = \dfrac{N_{\rm YSO}\,\langle M_{\rm YSO}\rangle}{\langle t_{\rm YSO}\rangle}$	$\mathrm{GDR_{Obs}} = \dfrac{M_{\rm gas}}{t_{\rm ff}^{\rm sph}}$
Theoretical	$\mathrm{SFR_{Theo}} = \left\langle \dot{M}_\star \right\rangle_{\Delta t}$	$\mathrm{GDR_{Theory}} = \sum_i \dfrac{m_{{\rm gas},i}}{t_{{\rm ff},i}}$
Mixed A	$\mathrm{SFR_{Theo}}$	$\mathrm{GDR_{Obs}}$
Mixed B	$\mathrm{SFR_{Obs}}$	$\mathrm{GDR_{Theory}}$

Notes: $\dot{M}_\star$ is the total stellar accretion rate averaged over a time window Δt. $t_{\rm ff}^{\rm sph}$ is the free-fall time assuming a uniform sphere. $\mathrm{GDR_{Theory}}$ uses per-particle free-fall times and mass. $\mathrm{SFR_{Obs}}$ corresponds to Class 0 YSO-counting assumptions with a fixed mean stellar mass ($\langle M_{\rm YSO}\rangle \approx 0.5\,M_\odot$) and a mean lifetime ($\langle t_{\rm YSO}\rangle \approx 0.5\,$Myr).

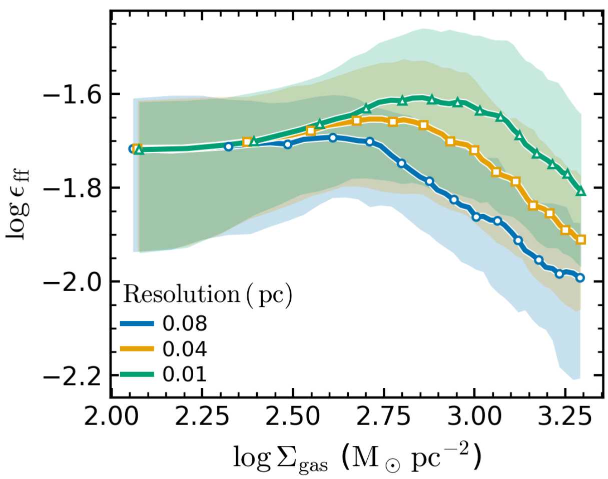

Figure 5. $\epsilon_{\rm ff}$ versus $\Sigma_{\rm gas}$ at three spatial resolutions: 0.01 pc (green), 0.04 pc (orange), and 0.08 pc (blue). The curves agree at low $\Sigma_{\rm gas}$ but diverge at high densities, where coarser resolutions smooth over compact gas around YSOs, lengthening free-fall times and lowering inferred efficiencies.

in low-mass and massive star-forming clouds. However, due to resolution constraints, star cluster formation simulations are often unable to resolve individual stars on massive GMC scales ($\gtrsim 10^4$ M$_\odot$) and therefore only include feedback from massive stars (P. Suin et al. 2024, e.g.,) or resolve individual star formation in collapsing low-mass star-forming clouds or regions ($\lesssim 10^3$ M$_\odot$) that do not form massive stars (e.g., S. S. R. Offner et al. 2009; C. Federrath 2015; A. J. Cunningham et al. 2018; S. M. Appel et al. 2023).

A key advantage of the simulations presented here is that STARFORGE properly models the formation of individual stars across the stellar mass spectrum (down to 0.1 M$_\odot$) on massive GMC scales ($\sim 10-100$ pc) and includes all feedback mechanisms inherent to star formation. This has allowed us to employ the methods from R. Pokhrel et al. (2021) for inferring the star formation rates determined from protostellar (Class 0) counts and estimated lifetimes (~ 0.5 Myr) motivated by prior observational studies (I. Evans et al. 2009; M. M. Dunham et al. 2014).

4.1. *Theoretical vs. Observational Interpretations of* $\epsilon_{\rm ff}$

In addition to stellar feedback, methodological choices are likely an important contributor to the divergence between theoretical and observationally inferred values of $\epsilon_{\rm ff}$. To examine this, we compare definitions directly (see Table 1), setting observational and theoretical formulations of star formation rates and gas depletion rates (GDRs) side by side, and introduce hybrid expressions to test where the two perspectives align or diverge. Our mixed approaches (Table 1, rows 3 and 4) act as diagnostics that isolate these effects. For example,

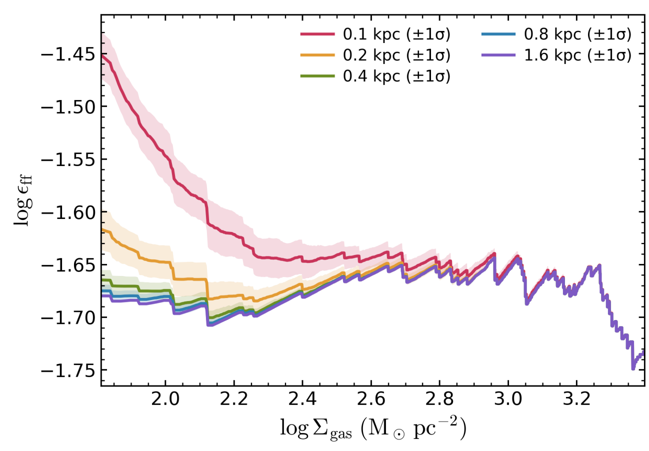

Figure 6. $\epsilon_{\rm ff}$ versus $\Sigma_{\rm gas}$ for clouds placed at distances of 0.1–1.6 kpc, with AGN injected at a surface density of 9 deg^{-2} (R. Pokhrel et al. 2020). At 0.1–0.4 kpc AGN contaminants elevate $\epsilon_{\rm ff}$ at $\log\Sigma_{\rm gas} \lesssim 2.5\,{\rm M_\odot\,pc^{-2}}$. The bias weakens with distance and is negligible by 1 kpc. The snapshot shown corresponds to $t \approx 6$ Myr.

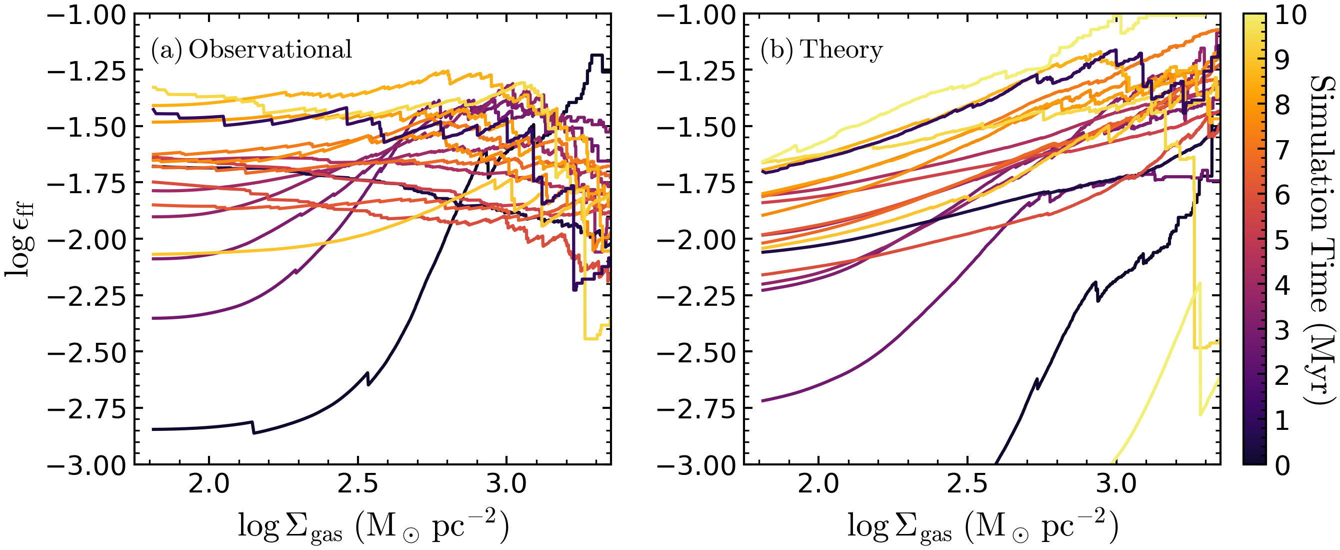

Figure 7. $\epsilon_{\rm ff}$ versus $\Sigma_{\rm gas}$ for the fiducial GMC over 3–10 Myr. (a) Observational approach used in this study. (b) Theory based on stellar accretion histories and multi–free-fall times. Curves are color-coded by cloud age, with purple denoting early times and yellow late times. The observational approach shows larger scatter, especially at low $\Sigma_{\rm gas}$, while the theoretical approach rises more systematically with $\Sigma_{\rm gas}$. This highlights how methodological choices shape inferred $\epsilon_{\rm ff}$ calculations.

Mixed Method A combines observational star formation rates, which assumes a common protostar mass estimate (0.5 $\rm M_\odot$) and Class 0 lifetime (0.5 Myr), with theoretical GDRs for each particle within the contour.

Figure 7 compares the different theoretical and observational estimates for $\epsilon_{\rm ff}$ described in Table 1. Both the observational estimates from our mock observations and "ground truth" theoretical values inferred directly from the simulation show scatter across the cloud's evolution. However, the theoretical values capture the systematic rise in $\epsilon_{\rm ff}$ at high densities that observations miss. This is likely due to the assumed protostellar masses or lifetimes commonly employed.

Figure 8 highlights this crossover, occurring around $\log \Sigma_{\rm gas} \approx 2.6\,\rm M_\odot\,pc^{-2}$, more clearly. Below this threshold, observational methods yield higher $\epsilon_{\rm ff}$ than theoretical estimates, consistent with Z. Hu et al. (2022), who show that spherical geometry assumptions systematically overestimate free-fall times. Above the threshold, the trend reverses. This surface density value marks the onset of massive star formation, where observational assumptions begin to fail. As stated above, YSO-based estimates typically assume a mean stellar mass of 0.5 $\rm M_\odot$, corresponding to the peak of the IMF, and a Class 0 lifetime of 0.5 Myr, yet massive protostars violate both assumptions through rapid accretion and shortened protostellar lifetimes due to fast Kelvin-Helmholtz contraction timescales (F. Motte et al. 2007; A. L. Rosen et al. 2016; A. L. Rosen 2022). As a result, the observational instantaneous star formation rates estimates are systematically underestimated in dense regions where massive stars preferentially form.

4.2. *Time-Dependent Evolution of* $\epsilon_{\rm ff}$

By taking into account the time evolution of star-forming GMCs, our results reveal that $\epsilon_{\rm ff}$ is not a static quantity. Following the evolution of $\epsilon_{\rm ff}$ as a function of both $\Sigma_{\rm gas}$ and time, we show that $\epsilon_{\rm ff}$ evolves dynamically throughout the cloud's life cycle. As shown in Figure 4, a single GMC exhibits significant scatter over its $\sim$10 Myr lifetime across different $\Sigma_{\rm gas}$ ranges, with episodic variations that challenge the interpretation of $\epsilon_{\rm ff}$ as a universal relation between gas supply and star formation.

Our results suggest that the scatter reported by R. Pokhrel et al. (2021) can be explained by evolutionary stage rather than intrinsic physical differences between GMCs. The variations within a single simulated cloud mirror those seen across surveys, reflecting that observations capture clouds at different points along a shared evolutionary track. Bursts of high efficiency are linked to massive star formation and the feedback it injects, underscoring their role in driving the evolution of $\epsilon_{\rm ff}$ which eventually reduces $\epsilon_{\rm ff}$ at late stages of the cloud's evolution before cloud dispersal occurs. As a result, attempts to link $\epsilon_{\rm ff}$ to specific mechanisms may be constrained unless the cloud's evolutionary state is explicitly considered. Recognizing this time dependence is therefore essential for connecting theoretical predictions with observational measurements of $\epsilon_{\rm ff}$.

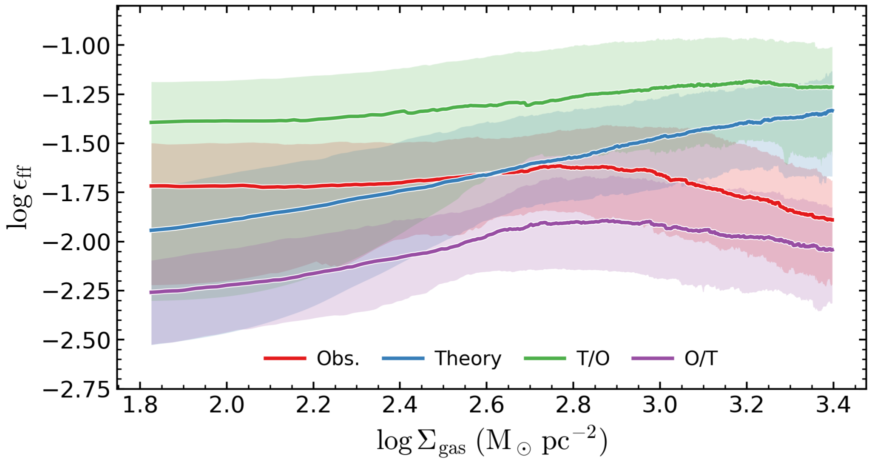

Figure 8. $\epsilon_{\rm ff}$ versus $\Sigma_{\rm gas}$ for different methodological definitions. Shaded regions show the 1σ scatter. The observational form (red) yields higher values at low $\Sigma_{\rm gas}$ due to geometric assumptions that shorten $t_{\rm ff}$, but falls below the theoretical form (blue) at higher densities, where indirect tracers undercount star formation. The two approaches cross near $\log \Sigma_{\rm gas} \sim 2.6\,{\rm M}_{\odot}\,{\rm pc}^{-2}$, marking a pivot before diverging at larger $\Sigma_{\rm gas}$. Hybrid forms (green, purple) combine numerators and denominators from each method, illustrating how geometry and tracer choice drive the offsets.

4.3. *Observational Biases*

Our mock observations reveal that FIR survey systematics strongly bias $\epsilon_{\rm ff}$, with resolution setting the largest bias and AGN contamination introducing a smaller but noticeable effect dependent on cloud distance. As shown in Figure 5, lowering the simulation spatial resolution systematically reduces the measured $\epsilon_{\rm ff}$ at high surface densities. Coarse resolution smooths compact structures around protostars, lowers peak surface densities, and shrinks dense contours, which redistributes YSOs and lowers observationally inferred estimates of $\epsilon_{\rm ff}$. Future FIR instruments with sub-0.1 pc resolution could alleviate this by resolving the small-scale structure around protostars, but current instruments lack this capability. Until then, observational studies must account for resolution smoothing or risk attributing instrumental limits to underlying physical mechanisms.

Beyond resolution constraints, AGN contamination introduces a smaller bias in our analysis. Shown in Figure 6, its influence is confined mainly to nearby clouds and lower-density regimes, where background sources can blend into YSO catalogs through their FIR emission. While this produces a modest upward shift in $\epsilon_{\rm ff}$ at the low end of $\Sigma_{\rm gas}$, the effect weakens with distance and becomes negligible compared to the resolution-driven biases. These results imply that resolution is the dominant observational bias in FIR studies of $\epsilon_{\rm ff}$, while AGN contamination plays only a secondary role. Accounting for both is critical for connecting observational measurements to theoretical predictions. Observers should remain mindful of these biases when interpreting efficiencies, and theorists applying observational techniques to simulations must do the same to ensure consistent comparisons.

4.4. *STARFORGE Limitations*

STARFORGE is the most physically complete simulation suite of star formation to date, but it still relies on assumptions and idealizations. The GMC is initialized as a uniform spherical cloud with a fixed mass, radius, metallicity, and uniform magnetic field strength, whose initial velocity distribution is seeded by turbulent motions. These idealized initial conditions does not capture the complex and poorly constrained assembly histories of real molecular clouds. As the simulation evolves, turbulence is allowed to freely decay rather than being continuously driven, unlike in the Milky Way where large-scale flows, feedback, and shear replenish it.

Additional physical processes are also treated simplistically, including the treatment of cosmic ray heating, grain-surface chemistry dust physics, and radiative transfer that employs an M1 solver and reduced speed of light approximation, which can underestimate radiation pressure in complex geometries. These choices keep the problem computationally feasible but can alter gas temperatures, abundances, and feedback strength, all of which feed into star formation rates and our inferred values of $\epsilon_{\rm ff}$. These limitations underscore the difficulty of modeling star formation in full detail but also help frame the scope of this study. STARFORGE provides a platform to test how feedback regulates $\epsilon_{\rm ff}$, with efficiencies that reach observed ranges without extreme initial conditions and evolve naturally over a cloud's lifetime.

5. CONCLUSION

In this work, we generated synthetic FIR observations of a high-fidelity RMHD STARFORGE simulation, which models massive star cluster formation via the gravitational collapse of a massive, turbulent GMC and includes self-consistent individual star formation and stellar feedback in the form of radiation, collimated outflows, and stellar winds. This approach has allowed us to directly apply observational techniques employed in FIR GMC star formation surveys, which rely on counting individual protostars, to determine the evolution of the observationally-inferred $\epsilon_{\rm ff}$ as a function of cloud evolution from the onset of star formation to cloud dispersal due to feedback. We find that stellar feedback regulates $\epsilon_{\rm ff}$, producing evolutionary variations in $\epsilon_{\rm ff}$ that are dependent on local cloud conditions and prior star formation. By comparing our observationally-inferred estimates of $\epsilon_{\rm ff}$ directly to the true star formation rates taken directly from the simulated outputs (i.e., the "ground truth") we were able to determine limitations that can arise from inferring $\epsilon_{\rm ff}$ from FIR star formation studies that often employ simplified assumptions, including assuming a fixed protostellar mass and lifetime to estimate the SFR of star forming clouds. We reach the following conclusions.

- $\epsilon_{\rm ff}$ varies strongly with surface density and cloud evolutionary state. In our high-resolution GMC simulation, efficiencies span over an order of magnitude (0.16–5.6%) across ∼10 Myr, naturally reproducing the low $\epsilon_{\rm ff} \approx 1-3\%$ values inferred from observations. This natural time dependence helps explain the scatter in surveys, demonstrating that $\epsilon_{\rm ff} \approx 1-3\%$ is regulated by stellar feedback and highly variable throughout the lifetimes of star-forming GMCs.

- We find that our theoretical estimates of $\epsilon_{\rm ff}$, taken directly from our simulated outputs are systematically different from our observationally-inferred estimates. Below $\log \Sigma_{\rm gas} \approx 2.6\ {\rm M_\odot pc^{-2}}$, observations overestimate $\epsilon_{\rm ff}$ due to spherical geometric assumptions applied to star-forming gas within GMCs, while at higher densities they underestimate the average protostellar mass and lifetimes yielding lower star formation rates.

- Limited resolution suppresses estimated $\epsilon_{\rm ff}$ in dense regions, while AGN contamination biases measurements in less dense regions of the cloud. Coarse resolution (0.08 pc vs. 0.01 pc) lowers efficiencies by up to 0.3 dex at high $\Sigma_{\rm gas}$, while AGN contamination produces smaller (<0.1 dex) effects in nearby clouds at low $\Sigma_{\rm gas}$.

This work demonstrates that synthetic observations of high-fidelity star cluster formation simulations that resolve individual star formation and stellar feedback on GMC scales provide a comprehensive framework that bridges theoretical and observational estimates of star formation metrics. Our pipeline reproduces the observed $\epsilon_{\rm ff}$ in Milky Way star-forming clouds while allowing us to follow this quantity throughout a GMC's lifetime. Our results suggest that the large scatter in observationally-inferred estimates of $\epsilon_{\rm ff}$ may not reflect intrinsic differences between clouds, but instead arises naturally from their evolutionary stage and observational biases.

ACKNOWLEDGMENTS

A.E. acknowledges support through the Carnegie Astrophysics Summer Student Internship (CASSI) San Diego State University's Undergraduate Research Program (SURP). A.E. thanks Anna Rosen (SDSU) and Michael Grudić (Flatiron Institute) for insightful conversations and guidance that shaped this work. The STARFORGE simulations used in this work were produced on the Frontera supercomputer at the Texas Advanced Computing Center (TACC), supported by the National Science Foundation (NSF) under grant OAC-1818253, and analyzed through the computational resources provided by the Flatiron Institute, supported by the Simons Foundation.

Software: STARFORGE (M. Y. Grudić et al. 2021), Gizmo (P. F. Hopkins 2017)

REFERENCES

Appel, S. M., Burkhart, B., Semenov, V. A., et al. 2023, ApJ, 954, 93, doi: 10.3847/1538-4357/ace897

Bastian, N., Covey, K. R., & Meyer, M. R. 2010, ARA&A, 48, 339, doi: 10.1146/annurev-astro-082708-101642

Bergin, E. A., & Tafalla, M. 2007, ARA&A, 45, 339, doi: 10.1146/annurev.astro.45.071206.100404

Chabrier, G. 2005, in Astrophysics and Space Science Library, Vol. 327, The Initial Mass Function 50 Years Later, ed. E. Corbelli, F. Palla, & H. Zinnecker, 41, doi: 10.1007/978-1-4020-3407-7_5

Crutcher, R. M. 2012, ARA&A, 50, 29, doi: 10.1146/annurev-astro-081811-125514

Cunningham, A. J., Krumholz, M. R., McKee, C. F., & Klein, R. I. 2018, MNRAS, 476, 771, doi: 10.1093/mnras/sty154

Dale, J. E. 2015, NewAR, 68, 1, doi: 10.1016/j.newar.2015.06.001

Dunham, M. M., Stutz, A. M., Allen, L. E., & et al. 2014, Protostars and Planets VI, 195, doi: 10.2458/azu_uapress_9780816531240-ch009

Evans, N. J., I., Dunham, M. M., Jørgensen, J. K., & et al. 2009, ApJS, 181, 321, doi: 10.1088/0067-0049/181/2/321

Federrath, C. 2015, MNRAS, 450, 4035, doi: 10.1093/mnras/stv941

Federrath, C., & Klessen, R. S. 2013, ApJ, 763, 51, doi: 10.1088/0004-637X/763/1/51

Goldreich, P., & Kwan, J. 1974, ApJ, 189, 441, doi: 10.1086/152821

Griffin, M. J., Abergel, A., Abreu, A., et al. 2010, A&A, 518, L3, doi: 10.1051/0004-6361/201014519

Grudić, M. Y., Guszejnov, D., Hopkins, P. F., Offner, S. S. R., & Faucher-Giguère, C.-A. 2021, MNRAS, 506, 2199, doi: 10.1093/mnras/stab1347

Grudić, M. Y., Guszejnov, D., Offner, S. S. R., et al. 2022, MNRAS, 512, 216, doi: 10.1093/mnras/stac526

Grudić, M. Y., Hopkins, P. F., Lee, E. J., et al. 2019, MNRAS, 488, 1501, doi: 10.1093/mnras/stz1758

Gutermuth, R. A., Megeath, S. T., Myers, P. C., & et al. 2009, ApJS, 184, 18, doi: 10.1088/0067-0049/184/1/18

Haworth, T. J., Glover, S. C. O., Koepferl, C. M., Bisbas, T. G., & Dale, J. E. 2018, NewAR, 82, 1, doi: 10.1016/j.newar.2018.06.001

Hensley, B. S., & Draine, B. T. 2023, ApJ, 948, 55, doi: 10.3847/1538-4357/acc4c2

Heyer, M., Krawczyk, C., Duval, J., & Jackson, J. M. 2009, ApJ, 699, 1092, doi: 10.1088/0004-637X/699/2/1092

Hopkins, P. F. 2017, arXiv e-prints, arXiv:1712.01294, doi: 10.48550/arXiv.1712.01294

Hopkins, P. F., & Raives, M. J. 2016, MNRAS, 455, 51, doi: 10.1093/mnras/stv2180

Hu, Z., Krumholz, M. R., Pokhrel, R., & Gutermuth, R. A. 2022, MNRAS, 511, 1431, doi: 10.1093/mnras/stac174

Kroupa, P. 2002, Science, 295, 82, doi: 10.1126/science.1067524

Krumholz, M. R. 2014, PhR, 539, 49, doi: 10.1016/j.physrep.2014.02.001

Krumholz, M. R., Dekel, A., & McKee, C. F. 2012, ApJ, 745, 69, doi: 10.1088/0004-637X/745/1/69

Lada, C. J., Lombardi, M., & Alves, J. F. 2010, ApJ, 724, 687, doi: 10.1088/0004-637X/724/1/687

Mac Low, M.-M., & Klessen, R. S. 2004, Reviews of Modern Physics, 76, 125, doi: 10.1103/RevModPhys.76.125

McKee, C. F., & Ostriker, E. C. 2007, ARA&A, 45, 565, doi: 10.1146/annurev.astro.45.051806.110602

Motte, F., Bontemps, S., Schilke, P., et al. 2007, A&A, 476, 1243, doi: 10.1051/0004-6361:20077843

Mouschovias, T. C., & Spitzer, Jr., L. 1976, ApJ, 210, 326, doi: 10.1086/154835

Offner, S. S. R., Klein, R. I., McKee, C. F., & Krumholz, M. R. 2009, ApJ, 703, 131, doi: 10.1088/0004-637X/703/1/131

Padoan, P., Federrath, C., Chabrier, G., et al. 2014, in Protostars and Planets VI, ed. H. Beuther, R. S. Klessen, C. P. Dullemond, & T. Henning, 77–100, doi: 10.2458/azu_uapress_9780816531240-ch004

Pokhrel, R., Gutermuth, R., Ali, B., et al. 2016, MNRAS, 461, 22, doi: 10.1093/mnras/stw1303

Pokhrel, R., Gutermuth, R. A., Betti, S. K., et al. 2020, ApJ, 896, 60, doi: 10.3847/1538-4357/ab92a2

Pokhrel, R., Gutermuth, R. A., Krumholz, M. R., et al. 2021, ApJL, 912, L19, doi: 10.3847/2041-8213/abf564

Rosen, A. L. 2022, ApJ, 941, 202, doi: 10.3847/1538-4357/ac9f3d

Rosen, A. L., & Krumholz, M. R. 2020, AJ, 160, 78, doi: 10.3847/1538-3881/ab9abf

Rosen, A. L., Krumholz, M. R., McKee, C. F., & Klein, R. I. 2016, MNRAS, 463, 2553, doi: 10.1093/mnras/stw2153

Sadavoy, S. I., Di Francesco, J., Johnstone, D., & et al. 2013, ApJ, 767, 126, doi: 10.1088/0004-637X/767/2/126

Suin, P., Zavagno, A., Colman, T., et al. 2024, A&A, 682, A76, doi: 10.1051/0004-6361/202347527

Zuckerman, B., & Evans, N. J., I. 1974, ApJL, 192, L149, doi: 10.1086/181613